



Cumene cracking over chromium oxide zirconia: Effect of chromium(VI) oxide precursors

N.H.R. Annuar^a, A.A. Jalil^{b,c}, S. Triwahyono^{a,d,*}, N.A.A. Fatah^b, L.P. Teh^a, C.R. Mamat^a

^a Department of Chemistry, Faculty of Science, Universiti Teknologi Malaysia, UTM, 81310 Johor Bahru, Johor, Malaysia

^b Institute of Hydrogen Economy, Universiti Teknologi Malaysia, UTM, 81310 Johor Bahru, Johor, Malaysia

^c Department of Chemical Engineering, Faculty of Chemical Engineering, Universiti Teknologi Malaysia, UTM, 81310 Johor Bahru, Johor, Malaysia

^d Ibnu Sina Institute for Fundamental Science Studies, Universiti Teknologi Malaysia, UTM, 81310 Johor Bahru, Johor, Malaysia



ARTICLE INFO

Article history:

Received 5 December 2013

Received in revised form 30 January 2014

Accepted 4 February 2014

Available online 12 February 2014

Keywords:

Cr₂O₃

ZrO₂

Chromium nitrate

Ammonium chromate

Cumene cracking

ABSTRACT

Two types of ZrO₂ supported with chromium nitrate (CN) and ammonium chromate (AC) for cumene catalytic cracking were studied. The physical properties of the catalysts were characterized with XRD, nitrogen physisorption, IR and TGA–SDTA. The acidic properties of the catalysts were determined by 2,6-lutidine and CO adsorbed IR spectroscopy. The XRD and nitrogen physisorption analyses confirmed higher tetragonal phase of ZrO₂ and specific surface area for Cr₂O₃–ZrO₂(AC) showing the ammonium chromate performed better interaction with Zr(OH)₄ than chromium nitrate. Besides, some of the chromium nitrate did not interact with Zr(OH)₄ and formed bulk crystalline Cr₂O₃ during the calcination. 2,6-lutidine and CO adsorbed IR spectroscopies distinguished that Cr₂O₃–ZrO₂(CN) possessed a stronger Lewis acid sites, while Cr₂O₃–ZrO₂(AC) possessed a stronger Brønsted acid sites. In situ IR spectroscopy demonstrated that Cr₂O₃–ZrO₂(CN) showed better interaction with a molecular hydrogen than Cr₂O₃–ZrO₂(AC) in the temperature range of 263–473 K. In addition, the bulk crystalline Cr₂O₃ interacted with a molecular hydrogen to form hydrogen bonded OH groups. At 523 K, the cumene hydrocracking indicated that the activity of Cr₂O₃–ZrO₂(CN) was about 1.7-fold higher than that of Cr₂O₃–ZrO₂(AC) with the main products of propylene and benzene. The high activity and stability of Cr₂O₃–ZrO₂(CN) were due to the better interaction with hydrogen molecules which generating high number of active protonic acid sites during the reaction. The activity of Cr₂O₃–ZrO₂(CN) is comparable with SO₄²⁻–ZrO₂ in the temperature range of 323–573 K.

© 2014 Elsevier B.V. All rights reserved.

1. Introduction

The operation of a modern refinery nowadays is becoming more complex. World-wide public concern about the earth's environment and health considerations led into several new legislative actions all around the world. With requirement to meet clean fuels challenge the processing configuration has to be adapted accordingly [1,2]. Focusing on petrol-fuel, several processes could be identified to perform hydrocarbon conversion such as cracking, alkylation and isomerization [3–5].

Zirconia (ZrO₂) is an oxide with high melting point (2973 K), high resistance for corrosion and low thermal conductivity material [6]. Thermal stability and surface properties of ZrO₂ can be

improved by admixtures of oxoanions of p and d elements such as chromate, carbonate, tungstate and molybdate [7–9]. They do not form bulk solutions with ZrO₂, but modify the properties of its surface. Previously, our research group reported the properties and acid catalytic testing of MoO₃–ZrO₂ [10]. We have suggested that the doublet IR bands at 1595 and 1580 cm⁻¹ corresponding to the tetragonal phase of ZrO₂ are responsible for the high activity of MoO₃–ZrO₂ in *n*-heptane isomerization. Whereas, the presence of Pt was crucial for Cr₂O₃–ZrO₂ to enhance the activity and stability of Cr₂O₃–ZrO₂ in cumene hydrocracking [11]. Pt facilitated the formation of protonic acid sites at doublets of 1675 + 1660 and 1650 + 1625 cm⁻¹ through a hydrogen spill over mechanism. For WO₃–ZrO₂, the heating of pyridine preadsorbed WO₃–ZrO₂ in the presence of hydrogen molecules decreased the intensity of the band at 1450 cm⁻¹ assigned to the Lewis acid sites and increased the intensity of the band at 1540 cm⁻¹ revealing the formation of active protonic acid sites [7]. Morterra et al. investigated the acidic sites of SO₄²⁻–ZrO₂ where the presence of tetragonal phase of ZrO₂ increased the activity of catalyst in *n*-butane

* Corresponding author at: Universiti Teknologi Malaysia, Ibnu Sina Institute for Fundamental Science Studies, Faculty of Science, 81310 UTM Johor Bahru, Johor, Malaysia. Tel.: +60 7 5536076; fax: +60 7 5536080.

E-mail addresses: sugeng@utm.my, sugengtw@gmail.com (S. Triwahyono).

isomerization [12]. While, Soultanidis et al. has concluded that the activity of $\text{WO}_x\text{-ZrO}_2$ was strongly affected by the nature of the support, calcinations temperature and its surface density [13]. For example, two types of $\text{WO}_x\text{-ZrO}_2$ were synthesized using commercially available amorphous $\text{ZrO}_x(\text{OH})_{4-2x}$ and model crystalline ZrO_2 as support precursors. WZrOH showed a maximum activity at the tungsten surface density of 5.2 W/nm^2 . In contrast, WZrO_2 which was prepared with crystalline ZrO_2 precursor was inactive in the reaction. Vaudagna et al. has explored the influences of tungsten oxide precursors on $\text{WO}_x\text{-ZrO}_2$ and $\text{Pt}/\text{WO}_x\text{-ZrO}_2$ [14]. The ammonium metatungstate and tungstic acid solution precursors were used to prepare $\text{WO}_x\text{-ZrO}_2$. The important difference was related to the migration of the precursor oxoanion into the narrowest pores of zirconium hydroxide, thus leading to different pore size distributions and amount of WO_3 particles on the catalyst. In addition, the presence of Pt was necessary to obtain the best catalytic activity and stability of $\text{WO}_x\text{-ZrO}_2$. Afanasiev et al. reported for ZrO_2 -supported Mo and W oxides prepared by conventional impregnation technique, molten salt method and calcinations of $\text{Zr}(\text{OH})_4$ impregnated with Mo(W) salt. They concluded that the solids which have been prepared by calcinations of impregnated $\text{Zr}(\text{OH})_4$ manifested the strongest Lewis and Brønsted acidity [15].

Although, large efforts have been undertaken to find a suitable catalyst and an effective process for the catalytic conversion of alkanes to more valuable hydrocarbon, fundamental study on the influence of precursors in the properties and activity of catalysts is still an interesting subject for developing new type of catalyst. In this study, we have prepared Cr_2O_3 loaded on ZrO_2 with different Cr_2O_3 precursors for cumene catalytic cracking. The influences of the precursors in the physical properties, acidity and catalytic activity are presented and discussed. The surface analyses showed that $\text{Cr}_2\text{O}_3\text{-ZrO}_2$ prepared with ammonium chromate solution (AC) possessed higher crystallinity, surface area and Brønsted acidity than that prepared with chromium nitrate (CN). In contrast, the chromium nitrate solution formed $\text{Cr}_2\text{O}_3\text{-ZrO}_2$ with strong Lewis acid sites and high ability to interact with a molecular hydrogen in the OH stretching and Cr=O stretching regions. These properties may differ the activity of $\text{Cr}_2\text{O}_3\text{-ZrO}_2$ (CN) and $\text{Cr}_2\text{O}_3\text{-ZrO}_2$ (AC) in the cumene catalytic cracking. The effects of the presence of bulk crystalline Cr_2O_3 in the activity of $\text{Cr}_2\text{O}_3\text{-ZrO}_2$ are also discussed.

2. Experimental

2.1. Catalysts preparation

Zirconium hydroxide was prepared from an aqueous solution of $\text{ZrOCl}_2\cdot 8\text{H}_2\text{O}$ (Wako Pure Chemical) by hydrolysis with $2.5\% \text{NH}_4\text{OH}$ (Merck) aqueous solution [7]. The final pH value of the supernatant was 9.0. The precipitate was filtered and washed with deionized water. The gel obtained was dried at 383 K to form $\text{Zr}(\text{OH})_4$. The chromium oxide loaded on zirconia ($\text{Cr}_2\text{O}_3\text{-ZrO}_2$) catalyst was prepared by incipient wetness impregnation technique at 353 K [16]. The aqueous chromium nitrate nanohydrate ($\text{Cr}(\text{NO}_3)_3\cdot 9\text{H}_2\text{O}$) or aqueous ammonium chromate ($(\text{NH}_4)_2\text{CrO}_4$) was impregnated on the $\text{Zr}(\text{OH})_4$, followed by drying overnight at 383 K and calcination at 873 K for 3 h in air. The catalysts are denoted as $\text{Cr}_2\text{O}_3\text{-ZrO}_2$ (CN) and $\text{Cr}_2\text{O}_3\text{-ZrO}_2$ (AC) for catalysts prepared with chromium nitrate nanohydrate and ammonium chromate precursors, respectively. The content of Cr_2O_3 was adjusted to 8 wt%. While, ZrO_2 was prepared by calcination of $\text{Zr}(\text{OH})_4$ at 873 K for 3 h in air.

The sulfate ion-treated $\text{Zr}(\text{OH})_4$, which is denoted as $\text{SO}_4^{2-}\text{-Zr}(\text{OH})_4$, was prepared by impregnation of the $\text{Zr}(\text{OH})_4$ with 1 N H_2SO_4 aqueous solution followed by filtration and drying at 383 K [9]. $\text{SO}_4^{2-}\text{-ZrO}_2$ was obtained by calcination of

$\text{SO}_4^{2-}\text{-Zr}(\text{OH})_4$ at 873 K for 3 h in air. The BET surface area of the catalyst was $120 \text{ m}^2/\text{g}$.

2.2. Characterization

X-ray diffraction (XRD) analysis was used to determine the crystallinity of the catalyst with a Bruker Advance D8 X-ray powder diffractometer with a $\text{Cu K}\alpha$ ($\lambda = 1.5418 \text{ \AA}$) radiation as a diffracted monochromatic beam at 40 kV and 40 mA. The data were collected at room temperature over the range of $2\theta = 2\text{--}40^\circ$ with a scan rate of 0.025° continuously. The fraction of tetragonal and monoclinic phases of ZrO_2 was determined based on Toraya equation [17].

$$V_t = 1 - \frac{1.31X_m}{1 + 0.31X_m} \quad (1)$$

$$X_m = \frac{I_m(1\ 1\ \bar{1}) + I_m(1\ \bar{1}\ 1)}{I_m(1\ 1\ \bar{1}) + I_m(1\ \bar{1}\ 1) + I_t(1\ 1\ 1)} \quad (2)$$

where X_m is the intensity ratio of monoclinic ZrO_2 . $I_t(1\ 1\ 1)$, $I_m(1\ 1\ 1)$ and $I_m(1\ 1\ \bar{1})$ are the integrated intensity of the (1 1 1) reflection of the tetragonal phase at $2\theta = 30.2^\circ$, (1 1 1) reflection of the monoclinic phase at $2\theta = 31.8^\circ$ and (1 1 $\bar{1}$) reflection of the monoclinic phase of ZrO_2 at $2\theta = 28.2^\circ$, respectively. While 1.31 is the Toraya's theoretical deviation from linearity value [17].

The BET specific surface area and pore distribution of the catalysts were determined by nitrogen physisorption with a Beckman Coulter SA 3100. Approximately 0.05 g of catalyst was put into a sample tube holder, followed by evacuation at 573 K for 3 h. The adsorption of nitrogen then was carried out at 77 K.

Thermal analysis TGA-SDTA of the catalysts were carried out using a Mettler-Toledo thermal analyzer, TGA/SDTA851e. The temperature of the furnace was set within the range of 298–1273 K with an increment of 5 K/min in a stream of nitrogen.

For measurement of the IR spectra, about 0.07 g catalyst was ground and pressed in a hydraulic press (5000 psi) in order to obtain 13 mm diameter of self-supporting wafer before placed in the purpose-made stainless steel IR cell with CaF_2 windows. The cell is connected to a vacuum-adsorption apparatus. Prior to the adsorption measurements, the catalyst was activated by heating at 598 for 1 h under oxygen stream followed by heating at 598 for 3 h under hydrogen stream and outgassing at 598 K for 3 h. The interaction of hydrogen and catalyst was observed in situ in the temperature range of 173–473 K where 13.3 kPa of hydrogen was introduced into the activated catalysts. While, 2,6-lutidine was used as a basic probe molecule for evaluating of the acidity of the catalysts, particularly in the observation of weak Brønsted acid sites and acidic centers of Lewis acid sites. The activated catalyst was exposed to 0.53 kPa of 2,6-lutidine at room temperature, followed by outgassing at room temperature and 373 K. In addition, carbon monoxide was also used as a basic probe molecule to evaluate the acidity of the catalyst where the weak electron-donating CO may form H-bonded complexes with the OH groups [18]. Partial pressure of 13.3 kPa was introduced into the activated catalyst at room temperature and 173 K. All spectra were recorded on an Agilent Cary 640 FTIR Spectrometer with a spectral resolution of 4 cm^{-1} and with 128 scans.

2.3. Cumene cracking

Cumene catalytic cracking was carried out in a microcatalytic pulse reactor at 323–573 K under hydrogen or nitrogen stream. Prior to the reaction, 0.4 g portion of the catalyst was charged into an ID10 mm tubular quartz glass reactor, and then it was subjected to O_2 treatment ($\text{O}_2 = 100 \text{ mL/min}$) at 673 K for 1 h, followed by H_2 reduction ($\text{H}_2 = 100 \text{ mL/min}$) at 673 K for 3 h. Then, the

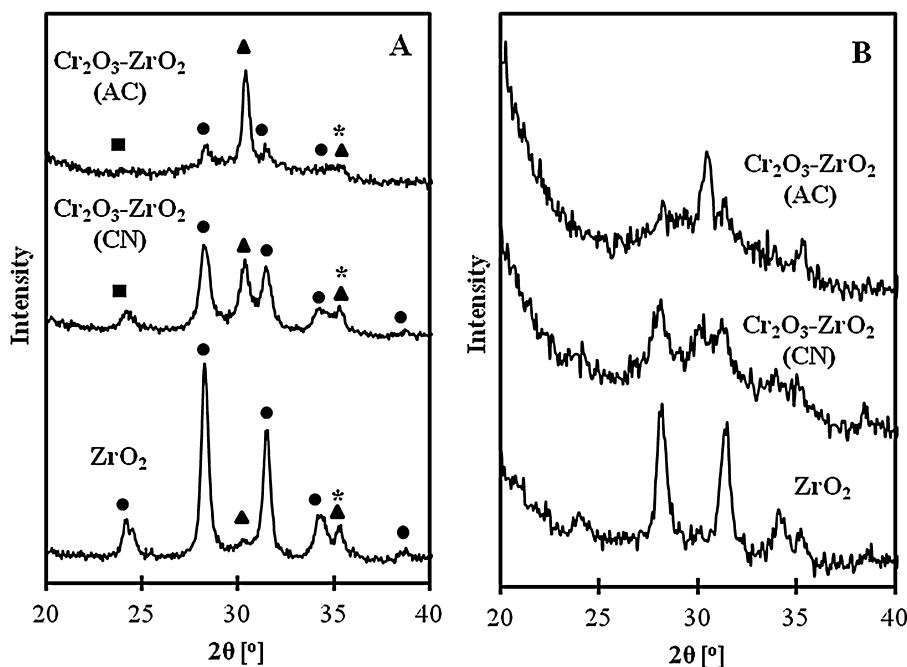


Fig. 1. X-ray diffraction patterns of (A) fresh and (B) activated ZrO_2 calcined at 873 K, $\text{Cr}_2\text{O}_3\text{-ZrO}_2$ (CN) and $\text{Cr}_2\text{O}_3\text{-ZrO}_2$ (AC); (●) monoclinic phase of ZrO_2 ; (▲) tetragonal phase of ZrO_2 ; (*) cubic phase of ZrO_2 ; (■) bulk crystalline Cr_2O_3 .

reactor was cooling down to a reaction temperature under the carrier gas stream. A dose of reactant ($14 \mu\text{mol}$) was passed over the activated catalyst and the products were trapped at 77 K before being flash-evaporated into an online 6090N Agilent Gas Chromatograph equipped with VZ7 packed Column and FID detectors. The intervals between doses were kept constant at 30 min. The reaction reached steady state at pulse number four (120 min). The activity of the catalyst was also evaluated in the reaction temperature range of 323–573 K.

The selectivity to particular product (S_i) and conversion of reactant (X_{reactant}) were calculated according to Eqs. (3) and (4), respectively.

$$S_i = \frac{C_i}{(\sum C_i) - C_{\text{res_reactant}}} \times 100; \quad (3)$$

$$X_{\text{reactant}} = \frac{(\sum C_i) - C_{\text{res_reactant}}}{(\sum C_i)} \times 100, \quad (4)$$

where C_i and $C_{\text{res_reactant}}$ are mole number of particular compound and residual reactant which was calculated based on the Scott hydrocarbon calibration standard gas (Air Liquide America Specialty Gases LLC).

3. Results and discussion

3.1. Physical properties of $\text{Cr}_2\text{O}_3\text{-ZrO}_2$ (CN) and $\text{Cr}_2\text{O}_3\text{-ZrO}_2$ (AC)

Fig. 1A illustrates the XRD patterns of fresh ZrO_2 , $\text{Cr}_2\text{O}_3\text{-ZrO}_2$ (CN) and $\text{Cr}_2\text{O}_3\text{-ZrO}_2$ (AC) calcined at 873 K. All catalysts exhibited three well established polymorphs of monoclinic, tetragonal and cubic phase of ZrO_2 . The diffraction peaks at $2\theta = 30.2^\circ$ and 35.5° attributed to the tetragonal phase of ZrO_2 , while the peaks at $2\theta = 24.2^\circ, 28.1^\circ, 31.4^\circ, 33.9^\circ$ and 38.4° attributed to the monoclinic phase of ZrO_2 [6,19]. A small peak at $2\theta = 35.2^\circ$ corresponds to the cubic phase of ZrO_2 [20]. There is also a weak and broad peak appeared at $2\theta = 24\text{--}25^\circ$ on $\text{Cr}_2\text{O}_3\text{-ZrO}_2$ (CN), assigned to bulk crystalline Cr_2O_3 , showing the existence of free chromium(VI) oxide on the surface of ZrO_2 which forming

a crystalline Cr_2O_3 during the calcinations [11]. While, almost no-peak corresponds to the bulk crystalline Cr_2O_3 was observed on $\text{Cr}_2\text{O}_3\text{-ZrO}_2$ (AC). In general, the presence of chromate anion which interacted with $\text{Zr}(\text{OH})_4$ inhibited the sintering of ZrO_2 crystallites and led to stabilize the tetragonal phase of ZrO_2 [7,21,22]. Table 1 presents the relative volume of monoclinic and metastable tetragonal phases of ZrO_2 (M/T) for the catalysts. ZrO_2 exhibited a highest ratio of monoclinic over tetragonal phase followed by $\text{Cr}_2\text{O}_3\text{-ZrO}_2$ (CN) and $\text{Cr}_2\text{O}_3\text{-ZrO}_2$ (AC). In fact, $\text{Cr}_2\text{O}_3\text{-ZrO}_2$ (AC) exhibited higher tetragonal phase at 30.2° than that of $\text{Cr}_2\text{O}_3\text{-ZrO}_2$ (CN), indicating the ammonium chromate has better interaction with $\text{Zr}(\text{OH})_4$. This may be due to the higher hydrophilicity of ammonium chromate than chromium nitrate nonahydrate [23]. The presence of monoclinic phase on ZrO_2 , $\text{Cr}_2\text{O}_3\text{-ZrO}_2$ (CN) and $\text{Cr}_2\text{O}_3\text{-ZrO}_2$ (AC) indicated that there existed free $\text{Zr}(\text{OH})_4$ hydroxyl groups on the catalyst which sintered to form monoclinic phase of ZrO_2 during the calcination. A similar result was reported by Trunschke et al. in which the monoclinic and tetragonal phase of ZrO_2 coexisted for 0.5–2 wt% chromium loading on ZrO_2 . While, the tetragonal modification of ZrO_2 predominated for 4 wt% chromium loading and above [24].

In addition to the fresh catalysts, Fig. 1B shows the XRD patterns of the activated ZrO_2 , $\text{Cr}_2\text{O}_3\text{-ZrO}_2$ (CN) and $\text{Cr}_2\text{O}_3\text{-ZrO}_2$ (AC) at 673 K. The ratio of the monoclinic to tetragonal phase of ZrO_2 was quite similar to the fresh catalysts, although the peaks became broader and lower in intensity. The changes were probably due to the inhomogeneous composition in a solid solution and smaller crystallite size in the crystalline materials after the activation process.

Nitrogen physisorption analysis showed that the BET specific surface areas of ZrO_2 , $\text{Cr}_2\text{O}_3\text{-ZrO}_2$ (CN) and $\text{Cr}_2\text{O}_3\text{-ZrO}_2$ (AC) were 42, 150 and $193 \text{ m}^2/\text{g}$, respectively (Table 1). This indicated that the introduction of Cr_2O_3 increased the surface area of the catalyst due to the formation of small diameter of pores in the catalysts. Whereas, the C (constant) values of ZrO_2 , $\text{Cr}_2\text{O}_3\text{-ZrO}_2$ (CN) and $\text{Cr}_2\text{O}_3\text{-ZrO}_2$ (AC) were 63.69, 55.10 and 54.86, respectively, showing the catalysts are oxide or mixture of oxide materials. In Fig. 2A, the N_2 adsorption–desorption isotherm could be classified as a

Table 1Properties of ZrO_2 , $\text{Cr}_2\text{O}_3-\text{ZrO}_2(\text{CN})$ and $\text{Cr}_2\text{O}_3-\text{ZrO}_2(\text{AC})$.

Sample	BET surface area [m^2/g]	Total pore volume [cm^3/g]	C (constant) value	Monoclinic/tetragonal phase of ZrO_2		Gaussian deconvolution area of 2,6-lutidine adsorbed FTIR	
				Fresh	Reduced (at 673 K)	$\text{Br}\ddot{\text{o}}\text{nsted acid sites}$ $1640 + 1630 \text{ cm}^{-1}$	Lewis acid sites $1567 + 1551 \text{ cm}^{-1}$
ZrO_2	42	0.162	63.69	83/17	82/18	–	–
$\text{Cr}_2\text{O}_3-\text{ZrO}_2(\text{CN})$	150	0.188	55.10	49/51	48/52	0.7799	2.2760
$\text{Cr}_2\text{O}_3-\text{ZrO}_2(\text{AC})$	193	0.172	54.86	25/75	24/76	3.0999	1.8400

type IV isotherm with the pore filling restricted to a range of $P/P_0 = 0.4-0.7$ assigned to mesoporous materials (intraparticles). The hysteresis loop was a H2 type indicating an agglomeration of uniform spheres with a complex mesoporous structure [25]. For $\text{Cr}_2\text{O}_3-\text{ZrO}_2(\text{CN})$, the size of the hysteresis loop was bigger than those of ZrO_2 and $\text{Cr}_2\text{O}_3-\text{ZrO}_2(\text{AC})$. This may be due to the bigger capillary condensation after adding the ammonium chromate precursor on the ZrO_2 . The amount of adsorbed nitrogen on $\text{Cr}_2\text{O}_3-\text{ZrO}_2$ increased by about 20% at $P/P_0 = 0$ than ZrO_2 indicating the introduction of Cr_2O_3 altered some mesoporous to a microporous structure. The increase was extensively observed on $\text{Cr}_2\text{O}_3-\text{ZrO}_2(\text{AC})$ than $\text{Cr}_2\text{O}_3-\text{ZrO}_2(\text{CN})$. Simultaneous decrease was observed at $P/P_0 = 0.9$, which reflects to the interparticle textural porosity [26].

Fig. 2B shows the pore size distribution of the catalysts where ZrO_2 has smaller total pore volume compared to both $\text{Cr}_2\text{O}_3-\text{ZrO}_2(\text{CN})$ and $\text{Cr}_2\text{O}_3-\text{ZrO}_2(\text{AC})$ (Table 1). A significant change in the mesopores was observed for $\text{Cr}_2\text{O}_3-\text{ZrO}_2(\text{CN})$ and $\text{Cr}_2\text{O}_3-\text{ZrO}_2(\text{AC})$ in which the loading of Cr_2O_3 decreased the numbers of pores with diameter of 5–10 nm and markedly increased the pore with diameter less than 5 nm. Inset figure shows that ZrO_2 demonstrated the presence of bigger pore volume in the range of 20–60 nm related to the higher nitrogen adsorption at $P/P_0 = 0.9$ indicating that higher partial pressure was associated with a smaller particle size and total pore volume [26]. Although, the total pore volume of $\text{Cr}_2\text{O}_3-\text{ZrO}_2(\text{AC})$ was slightly lower than that of $\text{Cr}_2\text{O}_3-\text{ZrO}_2(\text{CN})$, $\text{Cr}_2\text{O}_3-\text{ZrO}_2(\text{AC})$ has a higher surface area due to the higher number of micropore and external surface area which referring to the Cr_2O_3 metal deposition on the pores [27]. However, different results were observed on $\text{Cr}_2\text{O}_3-\text{Al}_2\text{O}_3$ in which Cherian et al. reported that the chromium nitrate formed catalyst

with higher surface area ($165 \text{ m}^2/\text{g}$) compared to the ammonium chromate ($145 \text{ m}^2/\text{g}$). In terms of the reactivity properties in the dehydrogenation of propane, $\text{Cr}_2\text{O}_3-\text{Al}_2\text{O}_3$ prepared with chromium nitrate exhibited higher selectivity than that of prepared with ammonium chromate.

The thermal behaviors of $\text{Zr}(\text{OH})_4$, $\text{Cr}_2\text{O}_3-\text{ZrO}_2(\text{CN})$ and $\text{Cr}_2\text{O}_3-\text{ZrO}_2(\text{AC})$ are represented in Fig. 3. Negative DTA peak indicated an endothermic process whereas the positive peak represented an exothermic process. The endothermic peak at about 340 K was a result of sample melting during dehydration as weight loss and water emission. The first weight loss showed by TGA curve arose in the range between 300 and 417 K due to the emission of water [28,29]. Another DTA peak at 465 K corresponds to the dehydroxylation of $\text{Zr}(\text{OH})_4$ produced an amorphous ZrO_2 . A small peak was also observed at 670 K which may correspond to the transformation of amorphous material into crystals [30]. DTA peaks at 770 and 940 K for both $\text{Cr}_2\text{O}_3-\text{ZrO}_2(\text{CN})$ and $\text{Cr}_2\text{O}_3-\text{ZrO}_2(\text{AC})$ may be due to the glow exotherm. It was found to be present in metal oxide which commonly attributed with the transition of an initially amorphous phase into a crystalline modification of ZrO_2 . The exothermal process probably corresponds to the crystallization of tetragonal metastable phase of ZrO_2 [31]. There was a small weight loss at high temperature showing the dehydroxylation process on both $\text{Cr}_2\text{O}_3-\text{ZrO}_2(\text{CN})$ and $\text{Cr}_2\text{O}_3-\text{ZrO}_2(\text{AC})$. In addition, the decrease of TGA curve was observed extensively on $\text{Cr}_2\text{O}_3-\text{ZrO}_2(\text{CN})$ which may associate with the continuous dehydration of the solid [32].

Fig. 4 presents the IR spectra in the OH groups stretching region at $3900-3000 \text{ cm}^{-1}$ when $\text{Cr}_2\text{O}_3-\text{ZrO}_2(\text{CN})$ and $\text{Cr}_2\text{O}_3-\text{ZrO}_2(\text{AC})$ were activated at different temperatures. When the catalysts were activated at 473 K, there were strong absorbance band at 3770 cm^{-1} , shoulder band at 3625 cm^{-1} and broad band in the

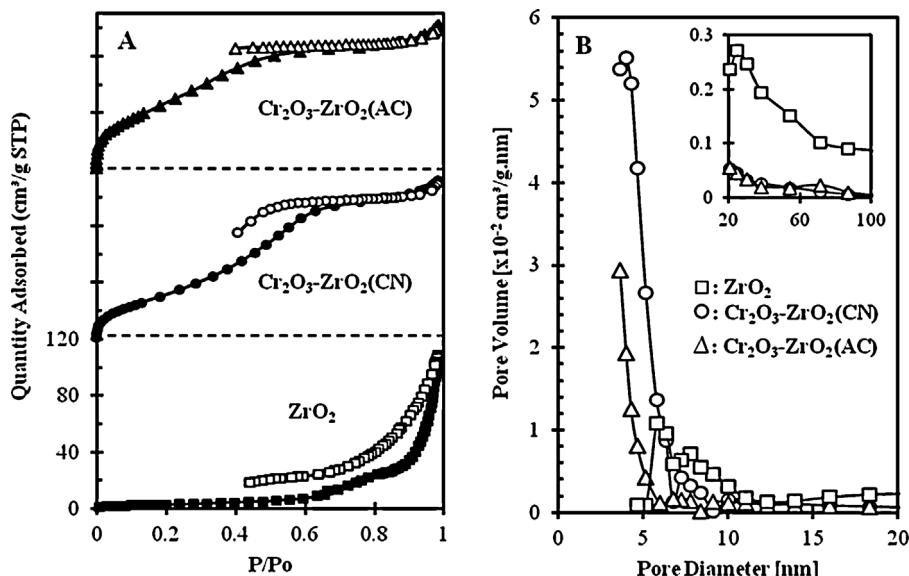


Fig. 2. (A) Nitrogen adsorption–desorption isotherm; solid symbol, adsorption; open symbol, desorption. (B) Pore size distribution of ZrO_2 , $\text{Cr}_2\text{O}_3-\text{ZrO}_2(\text{CN})$ and $\text{Cr}_2\text{O}_3-\text{ZrO}_2(\text{AC})$. Inset: pore diameter of 20–100 nm for the catalysts.

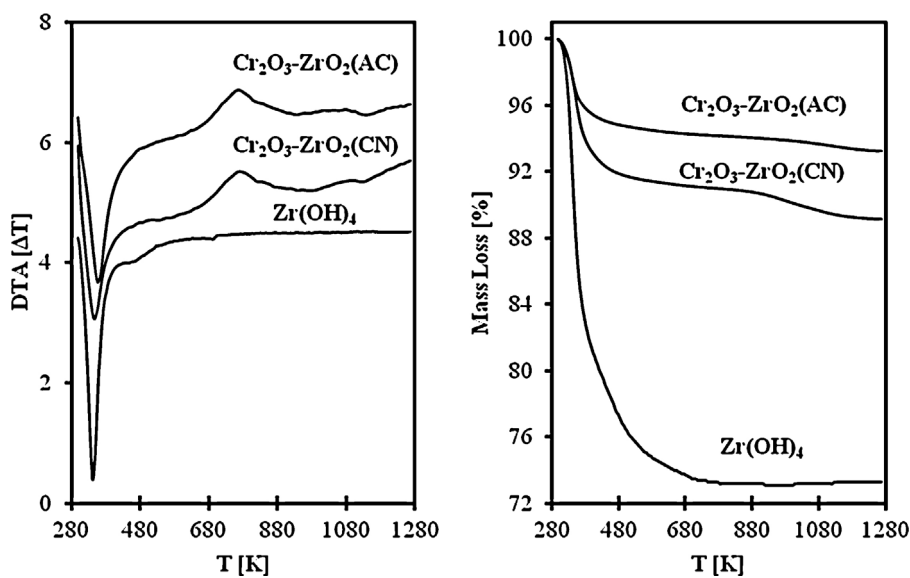


Fig. 3. DTA and TGA curves of $\text{Zr}(\text{OH})_4$, $\text{Cr}_2\text{O}_3\text{-ZrO}_2(\text{CN})$ and $\text{Cr}_2\text{O}_3\text{-ZrO}_2(\text{AC})$.

range of $3600\text{--}3000\text{ cm}^{-1}$ for both catalysts. The bands centered at 3770 and 3625 cm^{-1} showed the existence of several hydroxyl stretching bands with different acidic centers and strength. These bands were attributed to bibridged and tribridged OH groups correspond to the presence of tetragonal and monoclinic phases of ZrO_2 on the catalyst [33]. The high intensity of the bibridged OH groups on $\text{Cr}_2\text{O}_3\text{-ZrO}_2(\text{AC})$ signified the presence of higher tetragonal phase of ZrO_2 in accordance with the XRD result. Whereas the broad band in the stretching region of $3600\text{--}3000\text{ cm}^{-1}$ represented weak OH groups which interacted with some species or defect structure on the surface. At high activation temperature, this broad band disappeared, contrarily the bands centered at 3770 and 3625 cm^{-1} sharpened due to the removal of weak OH groups.

In addition, high activation temperature developed a new band centered at 3460 cm^{-1} attributed to the non-acidic OH groups for $\text{Cr}_2\text{O}_3\text{-ZrO}_2(\text{AC})$ [34]. Similar results were observed on $\text{WO}_3\text{-ZrO}_2$ [35] and $\text{MoO}_3\text{-ZrO}_2$ [10] in which increasing the activation temperature eliminated or decreased the OH groups at stretching region of $3800\text{--}3400\text{ cm}^{-1}$.

3.2. Interaction of hydrogen

Hydrogen molecules play an important role in the promotion effects of acid-catalyzed reaction where it can be rationalized by the formation of active protonic acid sites through a molecular hydrogen spillover phenomenon [36]. For example, the presence

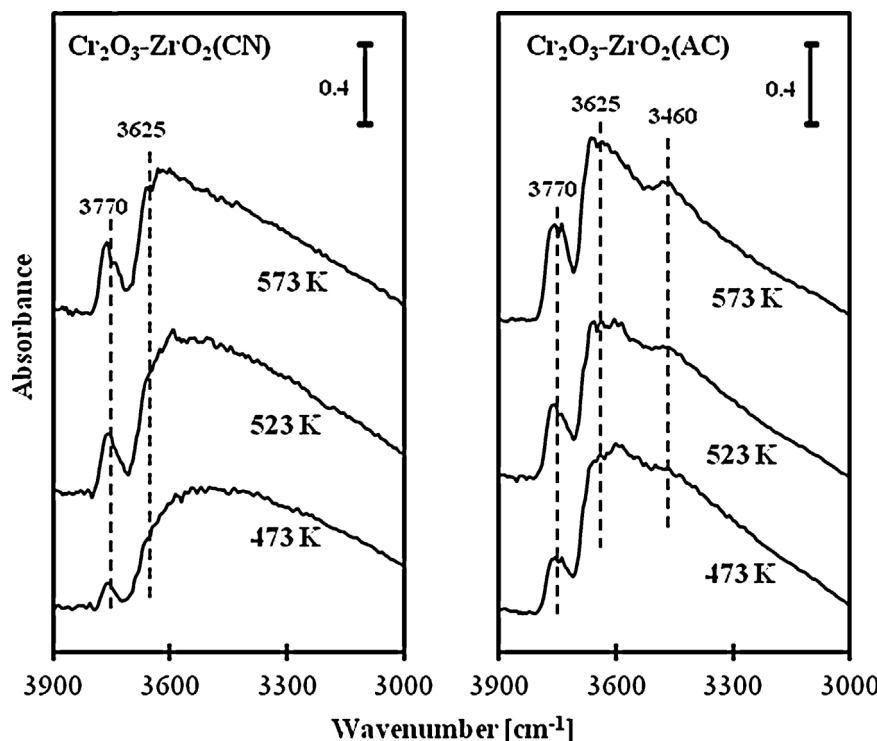


Fig. 4. IR spectra of activated $\text{Cr}_2\text{O}_3\text{-ZrO}_2(\text{CN})$ and $\text{Cr}_2\text{O}_3\text{-ZrO}_2(\text{AC})$. Samples were activated at 473, 523, and 573 K.

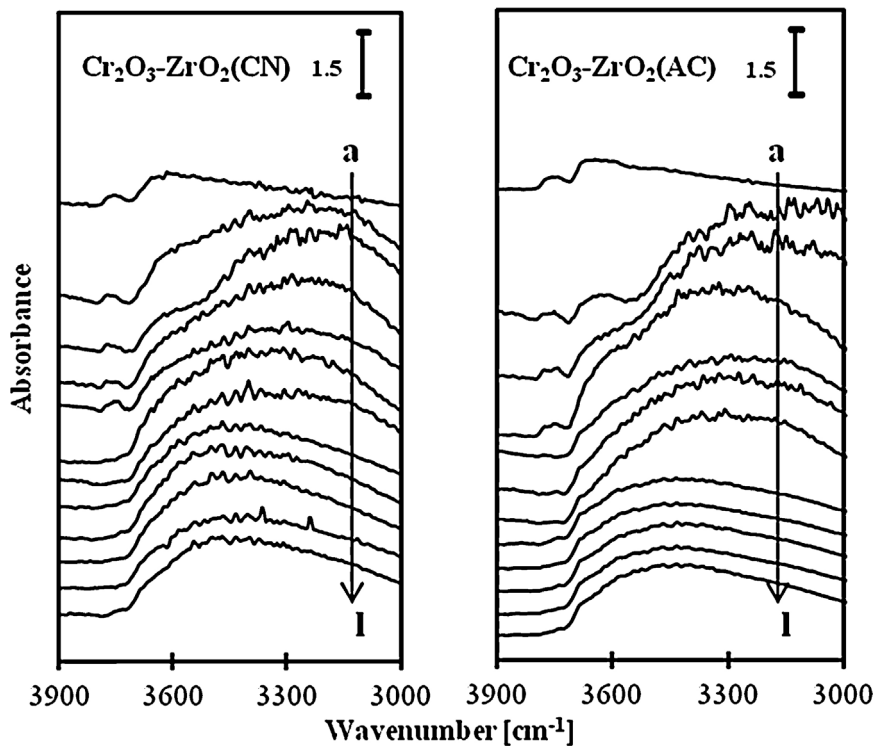


Fig. 5. IR spectra of activated $\text{Cr}_2\text{O}_3\text{-ZrO}_2(\text{CN})$ and $\text{Cr}_2\text{O}_3\text{-ZrO}_2(\text{AC})$ in the OH stretching region when the catalysts were exposed to 13.3 kPa hydrogen at 173 K, followed by heating at (b) 173 K, (c) 193 K, (d) 223 K, (e) 248 K, (f) 263 K, (g) 273 K, (h) 303 K (i) 323 K, (j) 373 K, (k) 423 K, and (l) 473 K. (a) The catalysts were activated at 598 K.

of molecular hydrogen enhances hydroisomerization and hydrocracking over $\text{SO}_4^{2-}\text{-ZrO}_2$, $\text{MoO}_3\text{-ZrO}_2$ and $\text{WO}_3\text{-ZrO}_2$ catalysts. The molecular hydrogen is adsorbed-desorbed on the specific active sites to form hydrogen atoms, followed by spillover onto the surface support to form acidic OH groups in which the acidic OH groups act as active sites in the reaction. In Figs. 5 and 6, the interaction of hydrogen molecules with the surface of $\text{Cr}_2\text{O}_3\text{-ZrO}_2(\text{CN})$

and $\text{Cr}_2\text{O}_3\text{-ZrO}_2(\text{AC})$ was observed in the OH stretching and Cr=O stretching regions in the temperature range of 173–473 K.

Fig. 5 shows the IR spectra of OH groups stretching region for molecular hydrogen interacted with the surface samples in the temperature range of 173–473 K. For all temperature range, only broad band corresponds to hydrogen bonded OH groups interacted with some species in the surface was observed for both

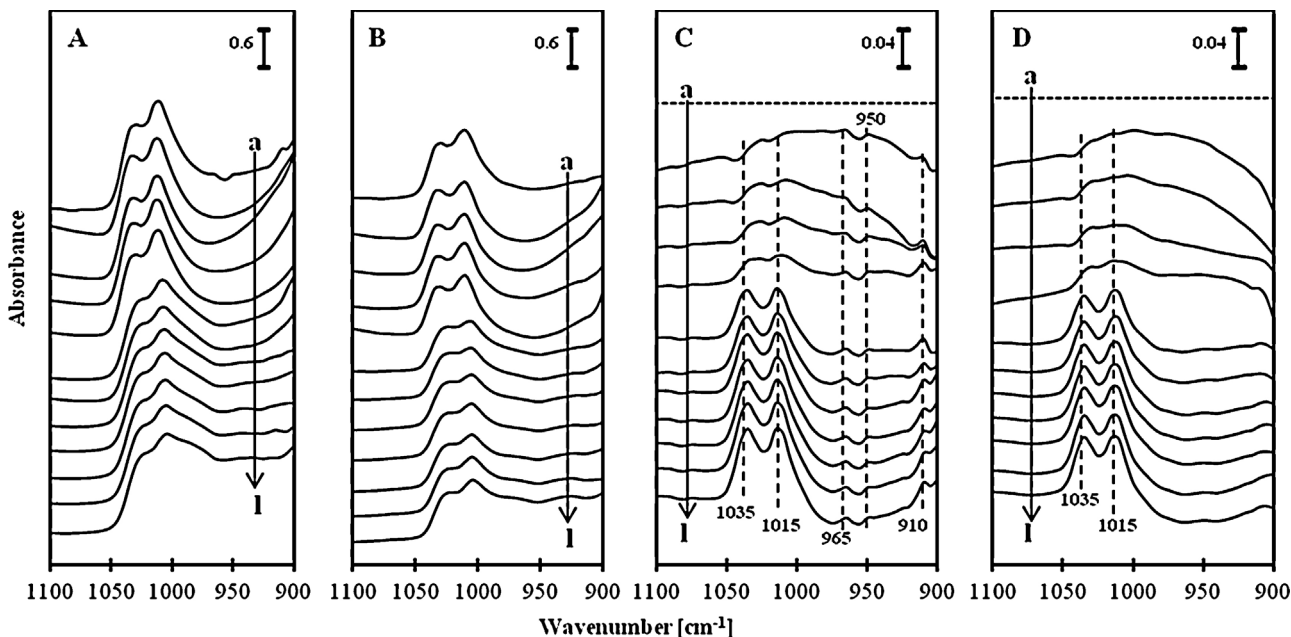


Fig. 6. IR spectra of (A) $\text{Cr}_2\text{O}_3\text{-ZrO}_2(\text{CN})$ and (B) $\text{Cr}_2\text{O}_3\text{-ZrO}_2(\text{AC})$ in the Cr=O stretching region when the catalysts were exposed to 13.3 kPa hydrogen at (b) 173 K, (c) 193 K, (d) 223 K, (e) 248 K, (f) 263 K, (g) 273 K, (h) 303 K (i) 323 K, (j) 373 K, (k) 423 K, and (l) 473 K. (a) The catalysts were activated at 598 K. (C) and (D) show the subtracted spectra of $\text{Cr}_2\text{O}_3\text{-ZrO}_2(\text{CN})$ and $\text{Cr}_2\text{O}_3\text{-ZrO}_2(\text{AC})$ in (A) and (B). The spectra were subtracted with the activated catalysts (spectrum (a) in (A) and (B)). Dotted lines; spectra of the subtracted activated samples.

$\text{Cr}_2\text{O}_3\text{-ZrO}_2(\text{CN})$ and $\text{Cr}_2\text{O}_3\text{-ZrO}_2(\text{AC})$. The adsorption of molecular hydrogen at 173 K may be conferred the physical adsorption of molecular hydrogen centered at 3200 cm^{-1} . Almost no-change was observed for the bibridged and tribridged OH groups. As the temperature increased, the absorbance band centered at 3200 cm^{-1} eroded and new broad band centered at 3550 cm^{-1} evolved. At and above 303 K, the absorbance band at 3200 cm^{-1} disappeared with a concomitant intensification in the broad and wide absorbance band centered at 3550 cm^{-1} . The evolution of the absorbance bands may be due to the alteration of the physical adsorption of molecular hydrogen at low temperature to the hydrogen bonded OH groups at relatively higher temperature [37]. The formation of the hydrogen bonded OH groups began to occur at 263 K on both catalysts indicating the adsorption and dissociation of molecular hydrogen to form hydrogen atoms occurred at relatively low temperature over both $\text{Cr}_2\text{O}_3\text{-ZrO}_2(\text{CN})$ and $\text{Cr}_2\text{O}_3\text{-ZrO}_2(\text{AC})$. In addition, the absorbance bands correspond to the bibridged and tribridged hydroxyl groups at 3770 and 3625 cm^{-1} shifted to a lower wavenumbers due to the inductive effect of hydrogen species coordinated to the *cus* Zr^{4+} sites in the vicinity of Cr_2O_3 [38]. A similar result was observed on the adsorption of molecular hydrogen over PtHZSM5 at 173–573 K in our previous assignment. The raising of the hydrogen adsorption temperature of PtHZSM5 eliminated OH groups at 3700, 3610 and 3520 cm^{-1} with a concomitant development of new OH groups at 3690, 3675, 3600 and 3380 cm^{-1} . This indicated that the adsorbed hydrogen species exhibited different characteristics as the temperature was varied. At 248 K, the adsorbed molecular hydrogen began to dissociate into atomic hydrogen species over the PtHZSM5 [39,40].

Fig. 6 illustrates the variations of IR spectra of activated $\text{Cr}_2\text{O}_3\text{-ZrO}_2(\text{CN})$ and $\text{Cr}_2\text{O}_3\text{-ZrO}_2(\text{AC})$ in the Cr=O stretching region in contact with molecular hydrogen at different temperatures. Curve (a) in Fig. 6A and B shows the spectra of the activated catalysts before hydrogen exposure in which both catalysts possessed bands at 1030 and 1010 cm^{-1} showing the presence of two independent Cr=O species. No-dioxo O=Cr=O species existed on the activated catalysts due to the absence of symmetric and antisymmetric stretching modes with different wavenumber of $30\text{--}50\text{ cm}^{-1}$ on both catalysts [35]. Another weak bands was observed at 965 , 950 and 910 cm^{-1} corresponding to the presence of bulk crystalline Cr_2O_3 on $\text{Cr}_2\text{O}_3\text{-ZrO}_2(\text{CN})$. No distinct band corresponds to the bulk crystalline Cr_2O_3 on $\text{Cr}_2\text{O}_3\text{-ZrO}_2(\text{AC})$. The changes of absorbance bands in contact with a molecular hydrogen in the temperature range of 173–473 K are shown in curve (b) to (l) in Fig. 6A and B. No significant changes of the spectra were observed at and below 248 K except small changes in the background line below 1000 cm^{-1} and the crystalline Cr_2O_3 bands. The background slightly lifted and the band of crystalline Cr_2O_3 disappeared showing the hydrogen species interacted with the surface of catalyst and crystalline Cr_2O_3 . The obvious changes were observed at and above 263 K in which the bands at 1030 and 1010 cm^{-1} decreased in intensity and shifted to lower frequencies of 1025 and 1005 cm^{-1} . Similar to those of the bibridged and tribridged OH groups, the shifting of Cr=O stretching bands to lower frequencies are due to the inductive effect of hydrogen species coordinated to the *cus* Zr^{4+} sites in the vicinity of Cr_2O_3 . In addition, a new broad and unresolved band was observed at $995\text{--}960\text{ cm}^{-1}$ attributed to the hydrogen bonded OH groups in the surface of catalysts. The alterations of the spectra caused by the hydrogen interaction are more clearly seen in Fig. 6C and D in which the spectra are subtracted with the activated catalyst.

Fig. 6C and D shows the subtracted IR spectra of Fig. 6A and B. All spectra were subtracted with the activated sample and dotted curve (a) in Fig. 6C and D shows the spectrum of subtracted spectra of activated sample. H_2 -exposure at low temperatures (173–248 K) for both catalysts showed a wide broad band at stretching region of $1050\text{--}900\text{ cm}^{-1}$ signifying the presence of hydrogen species

interacted with some species in the surface. Particularly, small absorbance band was observed at 1030 and 1010 cm^{-1} on both catalysts, while small bands at 965 , 950 and 910 cm^{-1} were only observed on the $\text{Cr}_2\text{O}_3\text{-ZrO}_2(\text{CN})$. The bands at 965 , 950 and 910 cm^{-1} is suggested to the hydrogen species coordinated to the bulk crystalline Cr_2O_3 . Significant changes were observed at and above 263 K in which the broad band at $1050\text{--}900\text{ cm}^{-1}$ eroded and the bands at 1030 and 1010 cm^{-1} shifted to 1035 and 1015 cm^{-1} . In addition, the bands at 965 , 950 and 910 cm^{-1} on the $\text{Cr}_2\text{O}_3\text{-ZrO}_2(\text{CN})$ intensified considerably. The changes may be corresponded to the alteration of the hydrogen species (hydrogen bonded $\text{H}_2\text{-O}$) to the hydrogen bonded OH groups at and above 263 K [41]. $\text{Cr}_2\text{O}_3\text{-ZrO}_2(\text{CN})$ showed a higher intensity of the bands at 1035 and 1015 cm^{-1} at high temperature, while $\text{Cr}_2\text{O}_3\text{-ZrO}_2(\text{AC})$ showed a higher intensity at low temperature. This result suggested that $\text{Cr}_2\text{O}_3\text{-ZrO}_2(\text{CN})$ interacted with more molecular hydrogen to form hydrogen bonded OH groups at high temperature than $\text{Cr}_2\text{O}_3\text{-ZrO}_2(\text{AC})$. In addition, the bulk crystalline Cr_2O_3 interacted with hydrogen species at wide range of adsorption temperatures. It can be suggested that molecular hydrogen dissociates on the reduced chromium species to form hydrogen atoms, and the hydrogen atoms migrate by spillover and diffusion on the $\text{Cr}_2\text{O}_3\text{-ZrO}_2$ surface where they are converted into protonic acid sites (H^+) and hydride (H^-). H^+ is formed by releasing an electron and stabilized on atomic O near the Lewis acidic center. ZrO_2 support (which Zr^{4+} being the Lewis site) traps an electron and then reacts with a second spillover hydrogen to form an H^- which bonded with the Lewis acid site [3]. It seems that the dissociation of H_2 does not occur on ZrO_2 or *cus* Zr^{4+} , since the interaction of H_2 and ZrO_2 does not form protonic acid sites and/or hydride. In fact, the presence of bulk crystalline Cr_2O_3 increased the interaction of H_2 and the surface of catalyst. Barton et al. signified that partly reduced WO_x domains on the ZrO_2 may act as redox sites required for the formation of H^+ species from H_2 . The lodging of a proton by electron transfer and charge delocalization across an extended W-O network results in electronic structures similar to those of heteropoly acids [42,43].

On the basis of the IR results in the present study together with the previous results reported on WO_3 loaded on ZrO_2 , it is suggested that the absorbance band at 1030 cm^{-1} on the $\text{Cr}_2\text{O}_3\text{-ZrO}_2$ corresponds to the stretching of the Cr=O which is connected to *cus* Zr^{4+} through O atom [35]. While, the band at 1010 cm^{-1} corresponds to the stretching of the Cr=O which is connected to the other Cr atom through O atom [35]. The spectra of $\text{Cr}_2\text{O}_3\text{-ZrO}_2$ are essentially the same to that of $\text{WO}_3\text{-ZrO}_2$ in our previous report in which two independent W=O species were observed at 1021 and 1014 cm^{-1} after the treatment at 673 K. We concluded that the IR bands at 1021 and 1014 cm^{-1} are assigned to the stretching of the W=O which is connected to *cus* Zr^{4+} through O atom and stretching of the W=O which is connected to the other W atom through O atom.

3.3. Intrinsic acidity of $\text{Cr}_2\text{O}_3\text{-ZrO}_2(\text{CN})$ and $\text{Cr}_2\text{O}_3\text{-ZrO}_2(\text{AC})$

2,6-Lutidine is known to be more sensitive probe on Brønsted acid site than pyridine due to its higher basicity and the steric hindrance of the methyl groups which can be used to study the relatively weak Brønsted acid sites and the acidic center of Lewis acid sites [44]. Fig. 7A and B shows 2,6-lutidine adsorbed on activated $\text{Cr}_2\text{O}_3\text{-ZrO}_2(\text{CN})$ and $\text{Cr}_2\text{O}_3\text{-ZrO}_2(\text{AC})$ at room temperature, followed by outgassing at room temperature and 373 K. There were six bands located at 1675 , 1660 , 1650 , 1640 , 1630 and 1625 cm^{-1} corresponding to the Brønsted acid sites and another set of six bands were located at 1607 , 1598 , 1593 , 1580 , 1567 and 1551 cm^{-1} corresponding to the Lewis acid sites. For the Brønsted acid region, strong doublet bands appeared at 1640 (8a mode) and 1630 (8b mode) cm^{-1} representing the protonated 2,6-lutidine species adsorbed

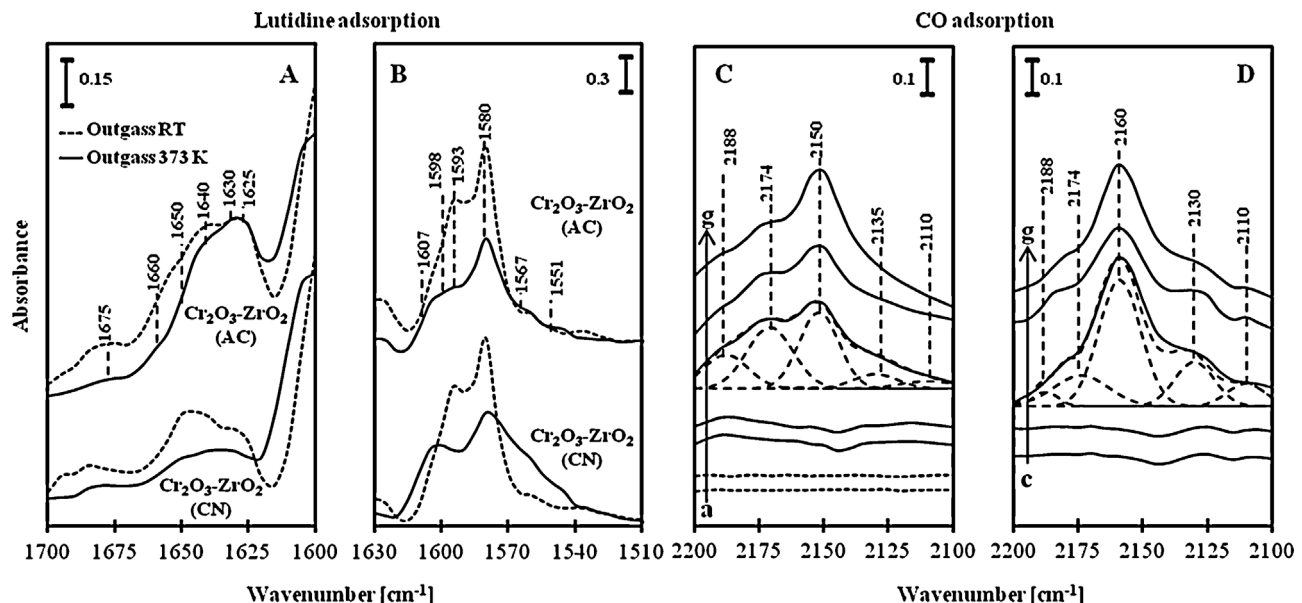


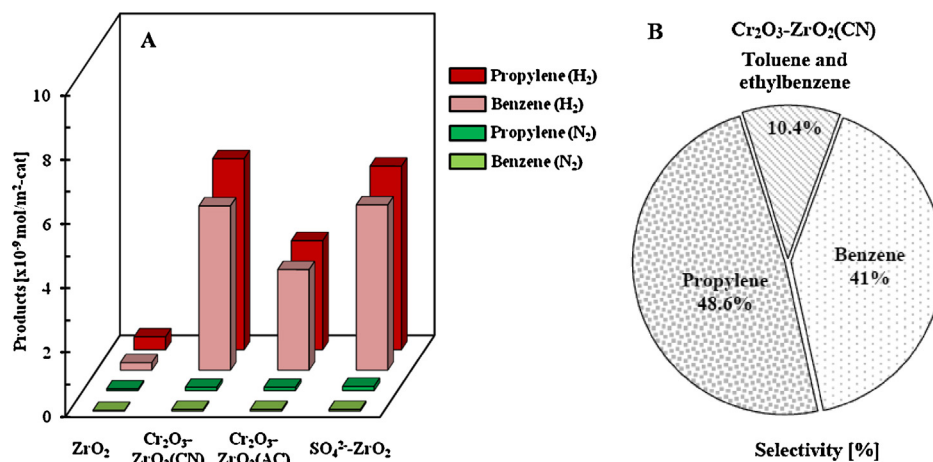
Fig. 7. IR spectra of 2,6-lutidine adsorbed on $\text{Cr}_2\text{O}_3\text{-ZrO}_2(\text{CN})$ and $\text{Cr}_2\text{O}_3\text{-ZrO}_2(\text{AC})$ at room temperature, followed by outgassing at room temperature (dotted lines) and 373 K (solid lines) at (A) Bronsted and (B) Lewis acid region. IR spectra of CO adsorbed on (C) $\text{Cr}_2\text{O}_3\text{-ZrO}_2(\text{CN})$ and (D) $\text{Cr}_2\text{O}_3\text{-ZrO}_2(\text{AC})$. The catalysts were activated at 598 K and CO was adsorbed at room temperature for (c) 3 min and (d) 5 min. CO was also adsorbed on the catalysts at 173 K for (e) 5 min, (f) 10 min and (g) 15 min. Dotted lines represent the adsorption of CO on ZrO_2 at (a) room temperature and (b) 173 K. Spectrum (e) shows the Gaussian deconvolution bands of the catalysts.

on Brønsted acid sites. Shoulder bands at 1675 and 1660 cm^{-1} were due to the 8a and 8b ring vibrational modes, whereas the bands at 1650 (8a mode) and 1625 (8b mode) cm^{-1} were assigned to the 2,6-lutidinium ions of Brønsted acid sites. For the Lewis acid region, dual doublets were observed, indicating H-bonded 2,6-lutidine corresponding to the monoclinic phase of ZrO_2 . The first of these bands was seen at 1607 (8a mode) and 1580 cm^{-1} (8b mode); the other was seen at 1593 (8a mode) and 1580 (8b mode) cm^{-1} . Furthermore, there were strong doublet bands corresponding to the tetragonal phase of ZrO_2 at 1598 (8a mode) and 1580 (8b mode) cm^{-1} . In addition, weak shoulder bands at 1567 (8a mode) and 1551 (8b mode) cm^{-1} corresponding to the tetragonal phase of ZrO_2 were also observed [12,45–47]. Upon heating in vacuum at 373 K, the progressive decrease was noted in the intensity of the bands attributed to the Lewis acid sites and only a slight decrease for the bands attributed to the Brønsted acid sites [45,46]. Particularly, when the catalysts were outgassed at 373 K, $\text{Cr}_2\text{O}_3\text{-ZrO}_2(\text{CN})$ exhibited stronger absorbance bands at 1567 and 1551 cm^{-1} compared to $\text{Cr}_2\text{O}_3\text{-ZrO}_2(\text{AC})$. This is suggested to be caused by the presence of bulk crystalline Cr_2O_3 or tetragonal phase of ZrO_2 accordance to the XRD analysis at $2\theta=24\text{--}25$ and 35.5° . Whereas, the band area of Brønsted acid sites at doublets of 1640 and 1630 cm^{-1} conferred higher value for $\text{Cr}_2\text{O}_3\text{-ZrO}_2(\text{AC})$ which may be due to the presence of large number of tetragonal phase of ZrO_2 . This signified that $\text{Cr}_2\text{O}_3\text{-ZrO}_2(\text{CN})$ possessed stronger Lewis acid sites and $\text{Cr}_2\text{O}_3\text{-ZrO}_2(\text{AC})$ possessed stronger Brønsted acid sites.

The use of strong base molecule such as 2,6-lutidine is known to have been suitable for probing at least the Brønsted and Lewis acidic groups of ZrO_2 based-catalyst. Besides, a small and weak electron-donating molecule such as carbon monoxide can also be utilized as a probe molecule to characterize the acidic groups through the H-bonding possibility. The carbon monoxide may form H-bonded complexes with the OH groups and be easily detected by IR spectroscopy following the absorption in OH and CO stretching regions. Fig. 7C shows no-band corresponding to CO for unmodified ZrO_2 at room temperature and 173 K (dotted lines). However, Morterra

et al. and Onfroy et al. reported their study of CO adsorption on ZrO_2 , $\text{SO}_4^{2-}\text{-ZrO}_2$ and $\text{WO}_3\text{-ZrO}_2$ at 77 K (temperature of boiling nitrogen), the bands at 2183 , 2158 and 2138 cm^{-1} correspond to CO stretching bands were observed on unmodified ZrO_2 [18,45]. The difference in the adsorption temperature of CO on ZrO_2 resulted a different result in which a low temperature of 77 K is necessary for the CO adsorption on ZrO_2 .

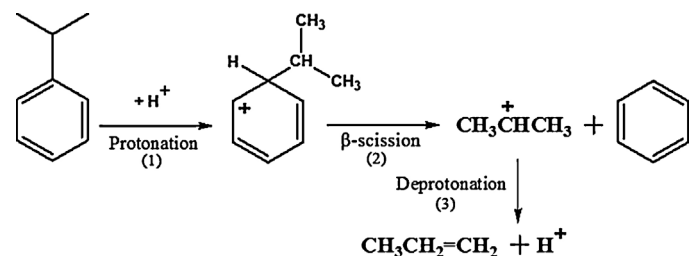
For the Cr_2O_3 loaded on ZrO_2 (Fig. 7C and D), no distinct absorbance bands were observed in the CO adsorption at room temperature for at least 5 min of CO-exposure. It is suggested that CO did not form H-bonded complexes with the OH groups at room temperature. So, the adsorptive interaction was studied at low temperature in order to reveal both strong and weak charge withdrawing center. At 173 K, the formation of a single broad and strongly asymmetric band centered at 2150 and 2160 cm^{-1} for $\text{Cr}_2\text{O}_3\text{-ZrO}_2(\text{CN})$ and $\text{Cr}_2\text{O}_3\text{-ZrO}_2(\text{AC})$, may be due to the interaction of the H-bonding type. Fig. 7C(e) and D(e) show the detail deconvolution bands of $\text{Cr}_2\text{O}_3\text{-ZrO}_2(\text{CN})$ and $\text{Cr}_2\text{O}_3\text{-ZrO}_2(\text{AC})$. Both catalyst have similar absorbance bands, but differ in the band positions. The bands were Lewis acid sites of ZrO_2 (L_{Zr} , 2188 cm^{-1}), Brønsted acid sites associated with chromate (B_{Cr} , 2170 and 2174 cm^{-1}) and ZrO_2 (B_{Zr} , 2160 and 2150 cm^{-1}) and physisorption at 2135 and 2130 cm^{-1} [48]. The band at 2110 cm^{-1} may correspond to the CO adsorption on *cus* Zr^{3+} [49]. The intensity of L_{Zr} , 2188 cm^{-1} for $\text{Cr}_2\text{O}_3\text{-ZrO}_2(\text{CN})$ is higher than that of $\text{Cr}_2\text{O}_3\text{-ZrO}_2(\text{AC})$ showing that $\text{Cr}_2\text{O}_3\text{-ZrO}_2(\text{CN})$ exhibited stronger Lewis acid sites. The intensity of the band did not change with the time of CO-exposure, indicating that the Lewis acid sites at 2188 cm^{-1} was strong acidic groups. Whereas, the intensity of the absorbance band corresponds to the Brønsted acid sites changed with the time indicating the presence of medium to strong acidic groups on both catalysts. The change was observed extensively on $\text{Cr}_2\text{O}_3\text{-ZrO}_2(\text{CN})$, showing that the $\text{Cr}_2\text{O}_3\text{-ZrO}_2(\text{CN})$ possessed weaker Brønsted acidic groups than that of $\text{Cr}_2\text{O}_3\text{-ZrO}_2(\text{AC})$. In addition to the stronger Brønsted acid sites, the $\text{Cr}_2\text{O}_3\text{-ZrO}_2(\text{AC})$ possessed higher number of acidic sites due to higher intensity of the band at 2160 cm^{-1} .



3.4. Cumene cracking

Cumene cracking was used to examine the activity of $\text{Cr}_2\text{O}_3\text{-ZrO}_2$ in the temperature range of 323–573 K. Previously, we have reported cumene catalytic cracking over Pt loaded on $\text{Cr}_2\text{O}_3\text{-ZrO}_2$ in which the presence of Pt markedly enhanced the activity and stability of $\text{Cr}_2\text{O}_3\text{-ZrO}_2$ [11]. In this report, the absence of the metal active site such as Pt is due to the elucidation of the intrinsic properties of Cr_2O_3 toward cumene catalytic cracking, particularly the effect of different Cr_2O_3 precursors in the acid catalytic reaction. Fig. 8A shows the comparison of cumene cracking activity over ZrO_2 , $\text{Cr}_2\text{O}_3\text{-ZrO}_2(\text{CN})$, $\text{Cr}_2\text{O}_3\text{-ZrO}_2(\text{AC})$ and $\text{SO}_4^{2-}\text{-ZrO}_2$ at 523 K in the presence of hydrogen or nitrogen carrier gas. No product was observed for the reaction in the absence of catalyst regardless to the carrier gas (data not shown). Trace amount of products were observed for the reaction in the presence of nitrogen carrier gas (in the absence of hydrogen) for all catalysts. In spite in the presence of hydrogen carrier gas, ZrO_2 showed low activity with the products of propylene and benzene were about 0.40 and 0.23 nmol/m²·cat, respectively. Whereas, $\text{Cr}_2\text{O}_3\text{-ZrO}_2(\text{CN})$ exhibited comparable activity to $\text{SO}_4^{2-}\text{-ZrO}_2$, but it was about 1.7-fold higher activity than that of $\text{Cr}_2\text{O}_3\text{-ZrO}_2(\text{AC})$. These results showed the indispensability of molecular hydrogen and specific active sites for assisting in the formation of active protonic acid sites for cracking process. Although, it is not certain at present, the reduced chromium species may act as a specific active site for assisting in the formation of active protonic active sites via hydrogen spillover phenomenon. In fact, almost no cracking product was observed either in the absence of hydrogen or chromium species indicating that the presence of permanent Brønsted acid sites has no role in the cumene catalytic cracking over $\text{Cr}_2\text{O}_3\text{-ZrO}_2$ type catalysts. While the presence of strong Lewis acid plays an important role in the stabilizing of formed protonic acid sites by trapping of electrons [50].

The product distribution of cumene hydrocracking over $\text{Cr}_2\text{O}_3\text{-ZrO}_2(\text{CN})$ is shown in Fig. 8B. The main products were propylene and benzene with the selectivity of 48.6 and 41%, respectively. About 10% was the by-products of toluene and ethylbenzene. Similar to the previous report on the cumene cracking over $\text{SO}_4^{2-}\text{-ZrO}_2$ [3], the cracking products were composed of benzene and propylene and no propane was formed. Although it is not shown here, the stability of $\text{Cr}_2\text{O}_3\text{-ZrO}_2(\text{CN})$ was observed for more than 100 pulses in which the reaction reached steady state at pulse number four. The cracking of cumene to propylene and benzene over $\text{Cr}_2\text{O}_3\text{-ZrO}_2$, is generally attributed to the interaction



Scheme 1. Proposed mechanism of cumene cracking over $\text{Cr}_2\text{O}_3\text{-ZrO}_2$.

of protonic acid site generated from molecular hydrogen as illustrated in Scheme 1. The mechanism of cumene cracking involves three following modes: (1) protonation at the ring carbon in which isopropyl group is attached, (2) beta-scission to form propyl cation and benzene and (3) deprotonation of propyl cation to form propylene and proton which will be used for the protonation at the ring carbon (1) [51–56].

Fig. 9 shows the main products of cumene hydrocracking at 523 K over $\text{Cr}_2\text{O}_3\text{-ZrO}_2(\text{CN})$ as a function of reaction temperature. The propylene and benzene products increased with increase in the reaction temperature indicating high temperature is necessary

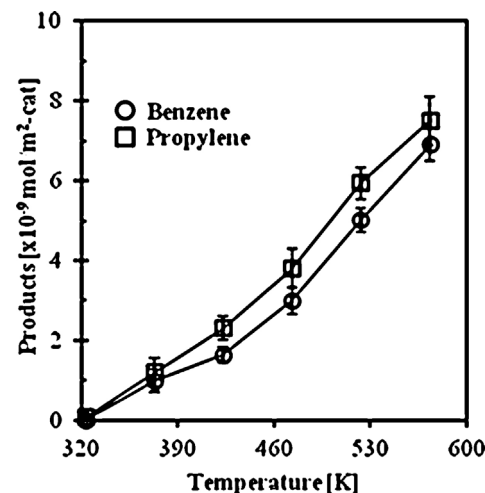


Fig. 9. Effect of reaction temperature in the product distribution of cumene hydro-cracking over $\text{Cr}_2\text{O}_3\text{-ZrO}_2(\text{CN})$.

for enhancing the cracking process due to the formation of more active protonic acid sites at a higher temperature. Sohn et al. [57], reported that the cracking reaction of *n*-hexane took place in strong acid sites of Cr_x–ZrO₂ while the active site for the dehydrocyclization reaction of *n*-hexane was Cr³⁺. The reactivity studies reveal that the activity of Cr₂O₃–ZrO₂ depends upon the type of structure of catalyst.

4. Conclusion

Cr₂O₃–ZrO₂ was successfully prepared with two different precursors of chromium nitrate (CN) and ammonium chromate (AC). The XRD and nitrogen physisorption analyses revealed that Cr₂O₃–ZrO₂(AC) possessed higher crystallinity and specific surface area than that of Cr₂O₃–ZrO₂(CN). This may be caused by the better interaction Zr(OH)₄ with ammonium chromate than chromium nitrate. In fact, some of the chromium nitrate did not interact with Zr(OH)₄ and formed bulk crystalline Cr₂O₃ on the surface during the calcination. The acidic properties of the catalysts confirmed that Cr₂O₃–ZrO₂(CN) has stronger Lewis and weaker Brønsted acid sites compared to Cr₂O₃–ZrO₂(AC). In addition, in situ IR spectroscopy revealed that Cr₂O₃–ZrO₂(CN) interacted with molecular hydrogen to form more hydrogen bonded OH groups than that of Cr₂O₃–ZrO₂(AC) at and above 263 K. Besides, the bulk crystalline Cr₂O₃ demonstrated an ability to interact with a molecular hydrogen to form hydrogen bonded OH groups on the surface. The higher hydrogen bonded OH groups led to exhibit the high activity Cr₂O₃–ZrO₂(CN) in cumene hydrocracking than that of Cr₂O₃–ZrO₂(AC). In addition, the activity of Cr₂O₃–ZrO₂(CN) is comparable with SO₄²⁻–ZrO₂ acid catalyst in the temperature range of 323–573 K.

Acknowledgments

This work was supported by the Universiti Teknologi Malaysia under The Research University Grant No. 04H26 and National Science Fellowship (N.H.R. Annuar) under the Ministry of Science, Technology and Innovation, Malaysia. Our gratitude also goes to the Hitachi Scholarship Foundation for the Gas Chromatograph Instruments Grant.

References

- [1] H. Weyda, E. Köhler, *Catal. Today* 81 (2003) 51–55.
- [2] F. Trejo, M.S. Rana, J. Ancheyta, A. Rueda, *Fuel* 100 (2012) 163–172.
- [3] T. Shishido, H. Hattori, *J. Catal.* 161 (1996) 194–197.
- [4] T. Kusakari, K. Tomishige, K. Fujimoto, *Appl. Catal., A* 224 (2002) 219–228.
- [5] K. Kubo, H. Iida, S. Namba, A. Igarashi, *Catal. Commun.* 29 (2012) 162–165.
- [6] B.M. Reddy, V.R. Reddy, *J. Mater. Sci. Lett.* 19 (2000) 763–765.
- [7] A.H. Karim, S. Triwahyono, A.A. Jalil, H. Hattori, *Appl. Catal., A* 433–434 (2012) 49–57.
- [8] S. Triwahyono, A.J. Aishah, S.N. Timmiati, N.N. Ruslan, H. Hattori, *Appl. Catal., A* 372 (2010) 103–107.
- [9] S. Triwahyono, Z. Abdullah, A.J. Aishah, *J. Nat. Gas Chem.* 15 (2006) 247–252.
- [10] N.N. Ruslan, N.A. Fadzillah, A.H. Karim, A.J. Aishah, S. Triwahyono, *Appl. Catal., A* 406 (2011) 102–112.
- [11] N.H.R. Annuar, A.A. Jalil, S. Triwahyono, Z. Ramli, *J. Mol. Catal. A: Chem.* 377 (2013) 162–172.
- [12] C. Morterra, G. Meligrana, G. Cerrato, V. Solinas, E. Rombi, M.F. Sini, *Langmuir* 19 (2003) 5344–5356.
- [13] N. Soultanidis, W. Zhou, A.C. Psarras, A.J. Gonzalez, E.F. Iliopoulos, C.J. Kiely, I.E. Wachs, M.S. Wong, *J. Am. Chem. Soc.* 132 (2010) 13462–13471.
- [14] S.R. Vaudagna, R.A. Comelli, N.S. Figoli, *Appl. Catal., A* 164 (1997) 265–280.
- [15] P. Afanasyev, C. Geantet, M. Breyssse, G. Coudurier, J.C. Vedrine, *J. Chem. Soc., Faraday Trans.* 90 (1994) 193–202.
- [16] M. Cherian, M.S. Rao, W.-T. Yang, J.-M. Jehng, A.M. Hirt, G. Deo, *Appl. Catal., A* 233 (2002) 21–33.
- [17] H. Toraya, S.J. Yoshimura, S. Somiya, *J. Am. Ceram. Soc.* 67 (1984) 119–121.
- [18] C. Morterra, G. Cerrato, S. Di Ciero, *Appl. Surf. Sci.* 126 (1998) 107–128.
- [19] L.F. Liotta, A.M. Venezia, G. Pantaleo, G. Deganello, M. Gruttaduria, R. Noto, *Catal. Today* 91–92 (2004) 231–236.
- [20] B.L. Kirsch, A.E. Riley, A.F. Gross, S.H. Tolbert, *Langmuir* 20 (2004) 11247–11254.
- [21] J.R. Sohn, S.G. Ryu, *Langmuir* 9 (1993) 126–131.
- [22] J.R. Sohn, S.G. Ryu, M.Y. Park, Y.I. Pae, J. Mater. Sci. 28 (1993) 4651–4659.
- [23] X. Huang, B. Hou, J. Wang, D. Li, L. Jia, J. Chena, Y. Sun, *Appl. Catal., A* 408 (2011) 38–46.
- [24] A. Trunschke, D.L. Hoang, J. Radnik, H. Lieske, *J. Catal.* 191 (2000) 456–466.
- [25] A.I. Trypolskyi, T.M. Gurnyk, P.E. Strizhak, *Catal. Commun.* 12 (2011) 766–771.
- [26] M.A.A. Aziz, A.A. Jalil, S. Triwahyono, R.R. Mukti, Y.H. Taufiq-Yap, M.R. Sazegar, *Appl. Catal., B* 147 (2014) 359–368.
- [27] F. Trejo, M.S. Rana, J. Ancheyta, *Ind. Eng. Chem. Res.* 50 (2011) 2715–2725.
- [28] S. Bianno, C. Badini, *J. Eur. Ceram. Soc.* 24 (2004) 3021–3034.
- [29] X. Turrillas, P. Barnes, D. Hausermann, *J. Mater. Chem.* 8 (1993) 163–168.
- [30] D.A. Ward, E.I. Ko, *Chem. Mater.* 5 (1993) 956–969.
- [31] P.D.L. Mercera, J.G. Van Ommen, E.B.M. Doesburg, A.J. Burggraaf, J.R.H. Ross, *Appl. Catal.* 57 (1990) 127–148.
- [32] E. Torres-Garcia, *J. Mater. Res.* 16 (2001) 2209–2212.
- [33] K.T. Jung, A.T. Bell, *J. Mol. Catal. A: Chem.* 163 (2000) 27–42.
- [34] L.H. Little, *Infrared Spectra of Adsorbed Species*, Academic Press, New York, NY, 1966.
- [35] S. Triwahyono, T. Yamada, H. Hattori, *Appl. Catal., A* 250 (2003) 75–81.
- [36] M.A.A. Aziz, N.H.N. Kamarudin, H.D. Setiabudi, H. Hamdan, A.A. Jalil, S. Triwahyono, *J. Nat. Gas Chem.* 21 (2012) 29–36.
- [37] V.B. Kazansky, A.I. Serykha, B.G. Andersonb, R.A. van Santen, *Catal. Lett.* 88 (2003) 3–4.
- [38] V.B. Kazansky, A.I. Serykha, *Catal. Lett.* 98 (2004) 2–3.
- [39] H.D. Setiabudi, A.A. Jalil, S. Triwahyono, N.H.N. Kamarudin, R.R. Mukti, *Appl. Catal., A* 417–418 (2012) 190–199.
- [40] H.D. Setiabudi, A.A. Jalil, S. Triwahyono, *J. Catal.* 294 (2012) 128–135.
- [41] H. Hattori, *Stud. Surf. Sci. Catal.* 138 (2001) 3–12.
- [42] E. Iglesia, D.G. Barton, J.A. Biscardi, M.J.L. Gines, S.L. Soled, *Catal. Today* 38 (1997) 339–360.
- [43] D.G. Barton, S.L. Soled, G.D. Meitzner, G.A. Fuentes, E. Iglesia, *J. Catal.* 181 (1999) 57–72.
- [44] A. Corma, C. Rodellas, V. Fornes, *J. Catal.* 88 (1984) 374–381.
- [45] T. Onfroy, G. Clet, M. Houalla, *J. Phys. Chem. B* 109 (2005) 3345–3354.
- [46] F. Leydier, C. Chizallet, A. Chaumonnot, M. Digne, E. Soyer, A. Quoineaud, D. Costa, P. Raybaud, *J. Catal.* 284 (2011) 215–229.
- [47] V. Lebarbier, G. Clet, M. Houalla, *J. Phys. Chem. B* 110 (2006) 13905–13911.
- [48] T.N. Vu, J. van Gestel, J.P. Gilson, C. Collet, J.P. Dath, J.C. Duchet, *J. Catal.* 231 (2005) 453–467.
- [49] Z.Y. Ma, C. Yang, W. Wei, W.H. Li, Y.H. Sun, *J. Mol. Catal.* 227 (2005) 119–124.
- [50] H.D. Setiabudi, A.A. Jalil, S. Triwahyono, N.H.N. Kamarudin, R. Jusoh, *Chem. Eng. J.* 217 (2013) 300–309.
- [51] S. Tiong Sie, *Ind. Eng. Chem. Res.* 31 (1992) 1881–1889.
- [52] S.N. Timmiati, A.A. Jalil, S. Triwahyono, H.D. Setiabudi, N.H.R. Annuar, *Appl. Catal., A* 459 (2013) 8–16.
- [53] K. Ebihara, J. Konishi, H. Hattori, *J. Catal.* 130 (1991) 257–267.
- [54] K. Ebihara, J. Tsuji, H. Hattori, H. Kita, *J. Catal.* 135 (1992) 607–609.
- [55] J.M. Parera, N.S. Figoli, *Catalytic Naphtha Reforming*, second ed., Marcel Dekker, New York, NY, 2004.
- [56] M.R. Sazegar, A.A. Jalil, S. Triwahyono, R.R. Mukti, M. Aziz, M.A.A. Aziz, H.D. Setiabudi, N.H.N. Kamarudin, *Chem. Eng. J.* 240 (2014) 352–361.
- [57] J.R. Sohn, S.G. Ryu, H.W. Kim, *J. Mol. Catal.* 135 (1998) 99–106.